

Article

## Insight into Rotational Effects on a Wind Turbine Blade Using Navier–Stokes Computations

Iván Herráez <sup>1,\*</sup>, Bernhard Stoevesandt <sup>2</sup> and Joachim Peinke <sup>1</sup>

<sup>1</sup> Forwind, University of Oldenburg, D-26111 Oldenburg, Germany; E-Mail: peinke@uni-oldenburg.de

<sup>2</sup> Fraunhofer Institute for Wind Energy and Energy System Technology, Ammerländer Heerstr. 136, D-26129 Oldenburg, Germany; E-Mail: bernhard.stoevesandt@iwes.fraunhofer.de

\* Author to whom correspondence should be addressed; E-Mail: ivan.herraez@forwind.de; Tel.: +49-441-798-5055.

External Editor: Frede Blaabjerg

Received: 31 July 2014; in revised form: 1 October 2014 / Accepted: 8 October 2014 /

Published: 21 October 2014

---

**Abstract:** Rotational effects are known to influence severely the aerodynamic performance of the inboard region of rotor blades. The underlying physical mechanisms are however far from being well understood. The present work addresses this problem using Reynolds averaged Navier–Stokes computations and experimental results of the MEXICO (Model Experiments in Controlled Conditions) rotor. Four axisymmetric inflow cases with wind speeds ranging from pre-stall to post-stall conditions are computed and compared with pressure and particle image velocimetry (PIV) experimental data, obtaining, in general, consistent results. At low angles of attack, the aerodynamic behavior of all of the studied blade sections resembles the one from the corresponding 2D airfoils. However, at high angles of attack, rotational effects lead to stall delay and/or lift enhancement at inboard positions. Such effects are shown to occur only in the presence of significant radial flows. Interestingly, the way in which rotational effects influence the aerodynamics of the MEXICO blades differs qualitatively in certain aspects from the descriptions found in the literature about this topic. The presented results provide new insights that are useful for the development of advanced and physically-sound correction models.

**Keywords:** Reynolds Averaged Numerical Simulation; CFD; rotational augmentation; radial pumping; stall delay; rotational effects; wind turbine aerodynamics

---

## 1. Introduction

The ever increasing size of wind turbine rotor blades requires accurate and efficient methods for the prediction of the aerodynamic loads and performance. Without a deep understanding of the flow phenomena governing the rotor aerodynamics, high levels of uncertainty must be expected within the design process, implying a reduction in cost-effectiveness and the reliability of the whole machine. Numerous difficulties have been identified in modeling the aerodynamics of rotor blades [1]. Even stationary axial inflow conditions lead to complex flow phenomena, which are not yet well understood. Flow separation, secondary flows and stall delay are examples of such interrelated phenomena, which furthermore are known to play a key role in the aerodynamic behavior of the rotor. Those effects, being highly three-dimensional (3D), limit substantially the applicability of two-dimensional (2D) airfoil polars for their use in the design process. Therefore, 2D polars need to be corrected for rotational effects before using them in aeroelastic codes and other design tools.

Simms *et al.* [2] reported the results of a blind test comparison in which different aerodynamic models were used for simulating the National Renewable Energy Laboratory (NREL) Unsteady Aerodynamics Experiment (UAE) Phase VI turbine. The computed results, which were obtained with numerical tools, ranging from blade element momentum (BEM) theory to wake and computational fluid dynamics (CFD) codes, showed a great level of uncertainty. The discrepancies observed between experiments and computations were attributed to the difficulty of predicting correctly the effect of rotation on rotor blades. This highlights the importance of improving the correction models for rotational effects, and at the same time, it stresses the necessity of gaining a deeper understanding of the underlying physical mechanisms.

The study of rotational effects dates back to the mid-20<sup>th</sup> century. Himmelskamp [3] studied experimentally the rotational effects on aircraft propellers and observed lift enhancement and stall delay in rotating blades as compared to non-rotating blades. Banks and Gadd [4] performed a theoretical analysis for steady boundary layers and inferred that rotation helps to delay stall, especially in the blade root region. McCroskey and Yaggy [5] showed that crossflows contribute to the delay of separation on rotating helicopter blades. A rotating and a non-rotating wind turbine blade were compared experimentally by Ronsten [6], concluding that rotational effects were significant only in the proximity of the hub. Wood [7] described stall delay in terms of pressure changes to the external inviscid flow and observed that it depends on the local solidity of the blades. The use of 3D steady momentum integral boundary layer equations allowed Du and Selig [8] to discern the importance of the Reynolds number for rotational effects on a wind turbine, deducing that for large wind turbines, rotational effects would be of less importance than for small turbines. Schreck and Robinson [9] investigated surface pressure measurements from the NREL UAE Phase VI experiment and observed that rotational augmentation is connected to radial surface pressure gradients. Tangler [10] also studied the experimental data from the same wind turbine and highlighted the importance of the trailing vorticity and rotational effects for the aerodynamic performance. An experimental work by Sicot *et al.* [11] on a small wind turbine, compared sectional surface pressure distributions from a rotating and a non-rotating blade operating in turbulent flow. The root region of the blade presented enhanced lift, but no evidence of stall delay was observed.

CFD simulations have also been commonly used since the last 15 years for the analysis of rotor aerodynamics. Different types of simulation codes have been validated against measurements since

then. Duque [12] and Duque *et al.* [13] obtained reasonable results (especially at attached flow conditions) simulating the NREL Combined Experiment Phase II and the NREL UAE Phase VI turbines with a Reynolds Averaged Numerical Simulation (RANS) unsteady compressible code that made use of overset grids and the Baldwin–Lomax algebraic turbulence model. Le Pape and Lecanu [14] used another unsteady compressible RANS code with the  $k\omega$  and the  $k\omega - SST$  turbulence models for simulating the NREL Phase VI turbine. The best results were obtained with the  $k\omega - SST$  model, but the predictions at stall conditions were rather inaccurate with both models. Johansen and Sørensen [15] used detached-eddy simulations (DES) based on the  $k\omega - SST$  turbulence model for predicting the flow around the NREL Phase VI turbine under parked conditions with fixed pitch, as well as with oscillating pitch. The DES results presented more three-dimensional flow structures than RANS simulations, but the global blade characteristics were not better predicted. Johansen and Sørensen [16] simulated three different wind turbines with RANS using the  $k\omega - SST$  model and one turbine using DES. The authors highlighted the challenges associated with the prediction of highly separated rotor flows. Sørensen *et al.* [17] obtained good results of the flow field upstream and downstream of the MEXICO (Model Experiments in Controlled Conditions) turbine in axial and yawed conditions using the  $k\omega$  turbulence model.

In general, most CFD codes obtained better results simulating the NREL UAE Phase VI turbine than the MEXICO turbine. Sørensen *et al.* [18] explained that the NREL turbine was comparatively well suited for the computation with the RANS method, because its blades are designed with the S809 airfoil, for which good results at high angles of attack (AoA) are obtained also with 2D simulations. Furthermore, that airfoil type is apparently rather insensitive to the vortex interaction in the wake, which facilitates its prediction with RANS. The authors also studied rotational effects in that wind turbine, concluding that the enhancement of the aerodynamic forces at inboard radial positions was attributed to radial pumping of the separated flow in the inboard blade region. In a later work, Schreck *et al.* studied the same turbine using RANS with the  $k\omega - SST$  turbulence model and ascribed the rotational effects to stationary vortical structures located on the upper blade surface [19]. Very recently, Guntur and Sørensen [20] studied the MEXICO turbine with RANS and the  $k\omega$  model, observing that on rotating blades there is a postponement of the separation point. Furthermore, it was concluded that the AoA at which separation is initiated is higher in 3D compared with 2D.

The knowledge gained from measurements, theoretical works and numerical computations has been used by several authors for developing correction models for 2D polars [21–28]. Breton *et al.* [29] compared six different correction models for rotational effects using a lifting-line prescribed wake vortex code for simulating the NREL UAE Phase VI turbine. None of the models was able to predict the measured data satisfactorily, and the loads under stall conditions were generally overestimated. Guntur *et al.* [30] performed a similar test with experimental data from the MEXICO wind turbine, using an inverse Blade Element Momentum method for determining the AoA. Again, none of the correction models was successful at predicting the 3D aerodynamic characteristics.

As shown, current knowledge about rotational effects is still incomplete and requires further investigation if rotor blades are to be designed in a more reliable and cost-effective way.

The present work addresses this problem using a CFD model of the MEXICO wind turbine in conjunction with experimental data. The existence of rotational effects is verified by comparing 2D

and 3D airfoil polars. Then, 2D and 3D  $C_p$  distributions are analyzed for ascertaining the mechanisms that lead to an augmentation of the lift force at inboard positions. A deeper insight into the sources of the rotational effects is gained through the study of distinctive flow features in the near wake and the boundary layer of the rotor blades. The knowledge gained from these analyses is compared throughout the paper with the findings from other studies and the assumptions from well-known correction models. This provides important information for the development of improved and physically-sound correction models.

## 2. Methods

### 2.1. The MEXICO Experiment

The EU FP5 MEXICO (Model Experiments in Controlled Conditions) project involved the extensive measuring of loads, surface pressure and flow field data of a three-bladed 4.5-m rotor diameter wind turbine placed in the Large Low-Speed Facility of the German-Dutch Wind tunnel, DNW, which has an open Section of  $9.5 \times 9.5 \text{ m}^2$  [31]. The blockage ratio was 18%, but the use of breathing slots behind the collector helped to reduce tunnel effects. Réthoré *et al.* [32] and Shen *et al.* [33] showed that tunnel effects have very limited influence on the rotor flow.

The design of the blades was based on three different aerodynamic profiles, as shown in Table 1.

**Table 1.** Airfoil type distribution along the span of the MEXICO (Model Experiments in Controlled Conditions) blade.

Radial Position [ $r/R$ ]	Airfoil Type
0.09–0.17	Cylinder
0.17–0.20	Transition
0.20–0.50	DU91-W2-250
0.50–0.54	Transition
0.54–0.70	RISØ-A1-21
0.70–0.74	Transition
0.74–1.00	NACA64-418

The blades were twisted and tapered, and a zig-zag tape at 5% of the chord was used both on the blade upper and lower surfaces to trigger the laminar to turbulent transition.

The tower was located 2.13 m downwind from the rotor, and its diameter was only 0.5 m; so, its influence on the rotor flow is believed to be negligible [33,34]. The measurements were performed under different inflow conditions. In this work, four wind speeds have been considered, namely 10, 15, 19 and 24 m/s. The rotational speed and the pitch angle were kept constant at 424.4 rpm and  $-2.3^\circ$ , respectively. Only axial inflow conditions are considered in order to isolate the rotational effects from other influences, like dynamic stall.

The pressure measurements were performed by means of pressure transducers placed at five different blade sections corresponding to the blade span positions 0.25R, 0.35R, 0.60R, 0.82R and 0.92R, where

R represents the rotor radius. Multiple PIV windows upstream and downstream of the turbine were used for measuring the flow field. Furthermore, the loads on the tower bottom were measured by means of a balance.

The tip speed was 100 m/s for all cases, meaning a tip speed ratio of 6.7 at design conditions ( $U_\infty = 15$  m/s). The Mach number did not exceed 0.3, and compressibility effects are consequently disregarded in this work.

Table 2 shows the chord-based Reynolds and Rossby numbers of the MEXICO turbine at different radial positions. For comparison with a large turbine, the same parameters corresponding to the NREL 5 MW wind turbine [35] are shown. In both cases, rated operating conditions have been assumed. The Reynolds number in the MEXICO turbine is one order of magnitude smaller than in the NREL 5 MW turbine, indicating that the viscous forces play a substantially stronger role in the MEXICO turbine. However, the Rossby number is similar for both machines (on average, it is just about 17% smaller in the MEXICO turbine), which implies that the effect of rotation in both cases is probably comparable. Furthermore, the Rossby number decreases towards the blade root, which in turn means that the influence of the Coriolis force in that blade region is stronger.

**Table 2.** Reynolds and Rossby numbers for the MEXICO (subscript MX) and the National Renewable Energy Laboratory (NREL) 5 MW (subscript NREL) wind turbines at different radial positions.

$r/R$	$Re_{MX}$	$Ro_{MX}$	$Re_{NREL}$	$Ro_{NREL}$
0.25	$4.3 \times 10^5$	2.9	$7.0 \times 10^6$	3.9
0.50	$5.5 \times 10^5$	7.4	$1.0 \times 10^7$	8.7
0.75	$6.2 \times 10^5$	14.1	$1.2 \times 10^7$	15.8
0.90	$6.2 \times 10^5$	20.1	$1.2 \times 10^7$	23.3

The MEXICO data set [36] also includes wind tunnel measurements of the 2D airfoils shown in Table 1. The Reynolds numbers from the 2D experiments are approximately in the range corresponding to the blades. Furthermore, the 2D airfoils were fitted with a zig-zag tape in the same fashion, like the blades for triggering the transition from laminar to turbulent flow. The 2D experiments include both lift and drag characteristics, as well as  $C_p$  distributions (except for the RISØ-A1-21 airfoil, for which only aerodynamic force coefficients are available).

It would be very useful to count with blade section characteristics obtained from parked rotor experiments in order to isolate rotational effects from possible 3D effects caused by the blade geometry. Such experiments were also carried out within the MEXICO project, but the corresponding measurement results are unfortunately not reliable, because of malfunctioning pressure sensors [37]. However, the main differences between 2D and 3D results are known to occur in the post-stall range, especially in the inboard region, where rotational effects clearly dominate over other influences [11,19]. Therefore, we assume that comparing 2D and 3D characteristics is an acceptable method for assessing the role of the rotational effects. This is also the most common way to do it [10,14,16,18,20,29,30,34,38].

Further details about the experimental set-up can be found in [36].

## 2.2. Numerical Method and Computational Mesh

The numerical results presented in this work have been obtained from incompressible steady-state Reynolds averaged Navier–Stokes (RANS) simulations performed with the open source software, OpenFOAM. OpenFOAM is a computational framework for numerical simulations of partial differential equations. The rotation of the system was accomplished using a non-inertial reference frame and adding the Coriolis and centrifugal forces to the momentum equations. The SIMPLE algorithm was employed for the pressure-velocity coupling. The convective terms were discretized with a second order linear-upwind scheme. The discretization of the viscous terms was achieved by means of a second order central-differences linear scheme. The spatial discretization was performed with the finite volume method. No time discretization was used, since only steady-state simulations were performed. The simulations were run fully turbulent and made use of the Spalart and Allmaras [39] turbulence model. The use of a so-called adaptive (also known as continuous) wall function allowed for the maintenance of a comparatively low number of cells without compromising the accuracy of the simulations under separated flow conditions. The way in which the adaptive wall function works is simple: it switches automatically between a low-Re and a high-Re computation approach in dependence of the local  $Y^+$  value. In regions where the first grid point is within the viscous sublayer (small  $Y^+$ ), the low-Re approach is followed, and the boundary layer is completely resolved. In areas where the first grid point is in the log-law region (high  $Y^+$ ), a wall function is used. A blending function is also implemented for the cases where the first grid point is within the buffer layer, *i.e.*, between the viscous sublayer and the log-law region. When the flow is separated or close to the separation point, the flow velocity becomes very low, which implies that  $Y^+$  will be also very small. The boundary layer will be then fully resolved instead of modeled with a wall function. This is a substantial enhancement as compared to standard wall functions, since it allows a satisfactory prediction of complex flow conditions, including stall [40–44].

In OpenFoam, the velocity-pressure coupling is based on a collocated grid approach (both the velocity and the pressure are solved at the center of the control volumes). This implies that both the velocity and the pressure conditions have to be defined at all boundaries. At the inlet, the wind speed was specified and the pressure was set to zero gradient. On the contrary, at the outlet, the pressure was predefined and the velocity was set to zero gradient. Non-slip boundary conditions were set for the blades and the nacelle.

The parallelization of the simulations was accomplished by means of the Message Passing Interface (MPI).

The iterative convergence was ensured by achieving at least three orders of magnitude reduction in the residuals of each field variable. Furthermore, in order to guarantee that the numerical results are grid independent, a grid convergence study was performed prior to carrying out the simulations presented in this paper. The study was based on the Grid Convergence Index (GCI) method developed by Roache [45,46], which is used for quantifying the numerical uncertainty. For this, the MEXICO rotor was simulated at design conditions (*i.e.*, 15 m/s and axisymmetric flow) with three different meshes. After generating a coarse mesh ( $5.8 \times 10^6$  cells), it was systematically refined for creating the medium ( $8.5 \times 10^6$  cells) and fine ( $11.3 \times 10^6$  cells) meshes.

Table 3 summarizes the results of the study for the key variables, torque and thrust.  $\phi$  represents the corresponding key variable, whereas  $e_{ext}$  and  $GCI$  represent the extrapolated relative error and the numerical uncertainty, respectively, both referring to the fine grid. The low uncertainty level obtained for both the torque and the thrust (0.42% and 0.55%, respectively) is a clear indicator that the results with the fine mesh are grid independent. That mesh was therefore used for all of the simulations presented in this paper.

**Table 3.** Results of the grid convergence study.

Parameter	$\phi = \text{Torque}$	$\phi = \text{Thrust}$
$\phi_{fine}$	101.97 Nm	569.97 N
$\phi_{medium}$	102.03 Nm	570.40 N
$\phi_{coarse}$	102.25 Nm	576.76 N
$e_{ext}$	0.34%	0.44%
$GCI$	0.42%	0.55%

The mesh exploited the 120-degrees symmetry of the wind turbine rotor by modeling only one blade. The domain consisted of 1/3 of a cylinder and employed periodic boundary conditions in order to account for the other two blades. Its length and radius were 52 and 16 m, respectively. The mesh was of a type that was unstructured and hex-dominant (99% of the cells were hexahedra ; the rest were split hexahedra). The boundary layer of the blades and the nacelle was resolved with five prism-layers. The use of the adaptive wall function allowed for a  $Y^+$  value on the blades between 50 and 200 under attached flow conditions, which helped to limit the number of cells. The wake and the regions where high gradients were expected were accordingly refined.

### 3. Results and Discussion

#### 3.1. 3D Aerodynamic Characteristics

As mentioned in Section 1, the aerodynamic characteristics extracted from rotating blades commonly present evidence of rotational effects, such as stall delay and lift enhancement (especially at radial positions close to the blade root). In order to verify the existence of such effects in the MEXICO turbine, the measured and computed lift coefficient ( $C_l$ ) characteristics from different blade radial positions are compared with experimental 2D  $C_l$  characteristics in Figure 1. The same comparison for the drag coefficient ( $C_d$ ) is shown in Figure 2. Every plot in those figures shows four points for the 3D experimental results. Every point corresponds to a different wind speed ( $U_\infty = 10, 15, 19$  and  $24$  m/s). Owing to the constant pitch angle and rotational speed, increasing wind speed implies increasing AoA. The full lines representing the numerical results were also obtained from the above-mentioned four free-stream wind speeds.

The 3D polars have been extracted from the numerical and experimental results following the method described in [16]. For this, the normal force coefficient ( $C_n$ ) and tangential force coefficient ( $C_t$ ) have been computed from the surface pressure coefficient ( $C_p$ ) distributions and then transformed into  $C_l$

and  $C_d$  after calculating the AoA. The calculation of the AoA is based on the method proposed by Hansen *et al.* [47], which relies on flow field data extracted from numerical simulations, and has proven to be reliable [16,18,48]. In this method, the wind speed is sampled along multiple rings both upstream and downstream of the rotor. The radius of the rings corresponds to the spanwise positions for which the AoA should be obtained. Then, the average velocity for each ring is calculated. Afterwards, the velocity in the rotor plane for each radius is computed by interpolating along the axial direction the mean velocities obtained in the previous step. Finally, the effective angle of attack is estimated with the following equation:

$$AoA = \arctan\left(\frac{U_{rotor}}{r\omega}\right) - \phi \tag{1}$$

where  $U_{rotor}$  is the axial wind speed in the rotor plane,  $\omega$  is the rotational speed,  $r$  is the local radius and  $\phi$  is the local angle between the chord of the blade section and the rotor plane, considering both the pitch and the twist angles.

**Figure 1.** Comparison of  $C_l$  characteristics at five different spanwise positions corresponding to (a) 0.25R, (b) 0.35R, (c) 0.60R, (d) 0.82R and (e) 0.92R. The dotted lines represent 2D experimental results; the circles indicate 3D experimental results and the full lines show 3D numerical results.

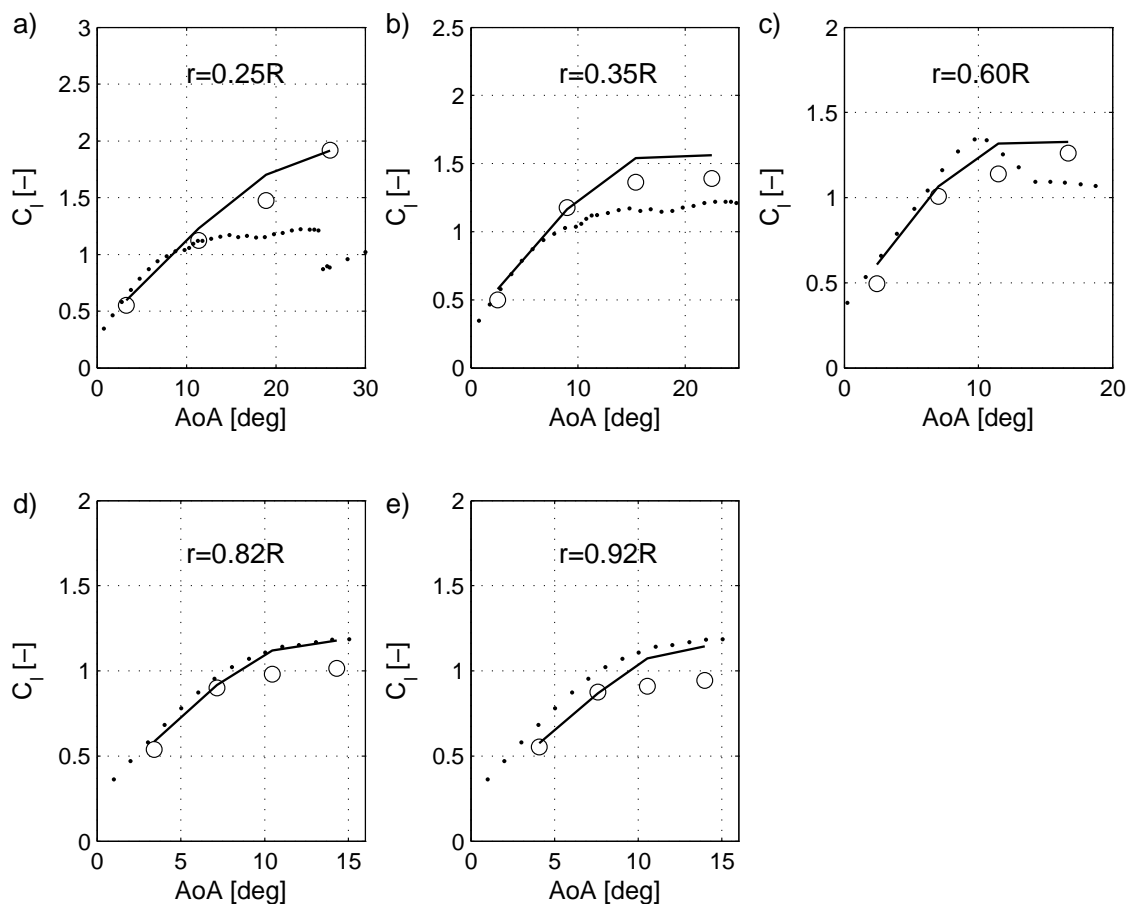
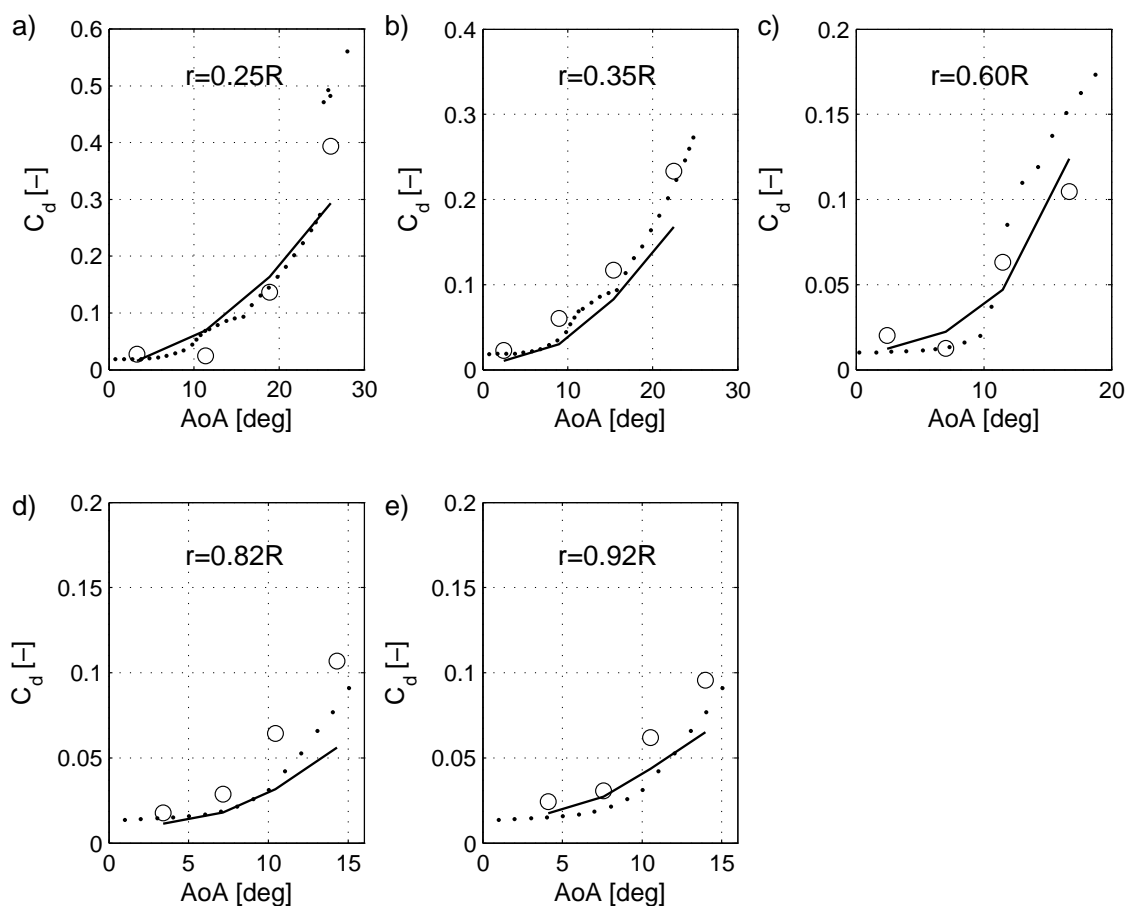


**Figure 2.** Comparison of  $C_d$  characteristics at five different spanwise positions corresponding to (a) 0.25R, (b) 0.35R, (c) 0.60R, (d) 0.82R and (e) 0.92R. The dotted lines represent 2D experimental results; the circles indicate 3D experimental results and the full lines show 3D numerical results.



### 3.1.1. 3D $C_l$ Characteristics

In the proximity of the blade root, *i.e.*, at  $r = 0.25R$  (Figure 1a), the experimental 3D  $C_l$  characteristics are almost identical to the 2D case until the 2D airfoil begins to stall (approximately at  $\text{AoA} = 12^\circ$ ). After having reached that angle, only the 3D  $C_l$  curve continues to rise. Indeed, that  $C_l$  curve does not present any evidence of stall for the whole range of available data, which goes until  $\text{AoA} = 26^\circ$ . Taking into account that the  $\text{AoA}$  of stall onset for the 2D case is approximately  $12^\circ$ , the lack of stall in the 3D case implies a delay in the stall  $\text{AoA}$  of at least  $14^\circ$ , *i.e.*, the stall onset is delayed by 117%. At  $\text{AoA} = 26^\circ$ , the 3D  $C_l$  curve presents 115% more lift than the 2D case for the same  $\text{AoA}$  and 55% more lift than the maximum lift from the 2D case. The simulations agree quite well with the measurements and are able to predict satisfactorily the stall delay and lift enhancement.

A bit further outboard, at  $r = 0.35R$  (Figure 1b), the experimental 3D  $C_l$  characteristics again resemble the 2D curve up to the 2D stall onset, although the slope of the 3D curve is slightly greater when the stall  $\text{AoA}$  is approached. At higher  $\text{AoA}$ , the 3D case presents lift enhancement as compared with the 2D curve. However, the slope of the 3D  $C_l$  characteristics becomes less steep after the 2D stall

onset, meaning that rotational effects are less strong at this position than at  $r = 0.25R$ . In fact, the stall angle does not seem to be delayed, in spite of the maximum lift being enhanced by approximately 15%. At this radial station, the numerical results are consistent with the 3D experimental results up to the 2D stall onset. For higher AoA, the simulations overpredict a bit the  $C_l$  values, although they offer a good qualitative agreement with the experiments.

In the proximity of the mid-span region, *i.e.*,  $r = 0.60R$  (Figure 1c), the experimental 2D and 3D  $C_l$  characteristics are similar until the stall onset. From the experimental results, it seems that at AoA = 12°, *i.e.*, shortly after the 2D stall onset, the rotating blade produces less lift than the 2D airfoil. However, at AoA = 17° (*i.e.*, in the post-stall region), the blade maintains almost the same  $C_l$  as the maximum  $C_l$  from the 2D airfoil, indicating the existence of stall delay. Measurements and simulations present a good qualitative and quantitative agreement for the whole range of available AoA, except for AoA = 12°, where the simulations overpredict the lift.

At  $r = 0.82R$  (Figure 1d) and more markedly at  $r = 0.92R$  (Figure 1e), the experimental 3D results display a lower  $C_l$  than the 2D airfoil for the whole range of AoA, although this effect is significantly stronger after the stall onset. At low AoA, the  $C_l$  reduction is attributed to the influence of the tip vortex on the local induction. At high AoA, there seems to exist an additional source of  $C_l$  reduction, which is discussed later in more detail. The simulations predict satisfactorily the linear range, but overestimate  $C_l$  at high AoA. Here, it is worth recalling that other CFD investigations from the MEXICO turbine encountered the same difficulties in the outboard region. As an example, the final report of the MexNext project [49] shows a comparison of the  $C_p$  distributions obtained from different CFD models. At  $U_\infty = 24$  m/s, the results for  $r = 0.82R$  and  $r = 0.92R$  from six different models out of seven present a good consistency between them. However, all of the mentioned models overpredict the negative pressure on the attached flow region of the suction side, which implies an overestimation of  $C_l$ .

Breton *et al.* [29], who used a lifting line prescribed wake vortex code for simulating the NREL UAE Phase VI turbine, documented that most correction models for rotational effects lead to an overprediction of the lift in the outermost region of the blade. Only two exceptions were identified: the model by Corrigan and Schillings [26], who suggested not to apply any correction for rotational effects above  $r = 0.75R$ , and the model by Lindenburg [25], who suggested not only not to apply any lift-enhancement correction above  $r = 0.80R$ , but also to introduce a special tip loss correction for accounting for radial flows above that radial position. The results from the MEXICO turbine confirm that it is a good idea to limit the enhancement of the lift force at outboard positions. The suitability of the special tip loss correction proposed by Lindenburg is discussed later in connection with the drag.

### 3.1.2. 3D $C_d$ Characteristics

In opposition to the 3D  $C_l$  characteristics, the 3D  $C_d$  characteristics (Figure 2) are more or less in good agreement with the 2D characteristics at  $r = 0.25R$  and  $r = 0.35R$  for the whole range of available AoA (even under stall conditions). The simulations are in general consistent with the experiments, except at the highest AoA, where  $C_d$  is underestimated. Furthermore, at  $r = 0.35R$ , the simulations tend to slightly underestimate  $C_d$  for the whole range of AoA.

At  $r = 0.60R$  (Figure 2c), the experimental 3D  $C_d$  characteristics resemble again the 2D case, except at AoA = 17°, where the 3D drag is reduced as compared with the 2D case. As it was seen in the  $C_l$

characteristics for the same radial position and AoA, rotational effects play a significant role at these conditions. The  $C_d$  reduction is therefore attributed to the mentioned effects. The numerical results are also reasonably consistent with the experiments at this station. At  $AoA = 17^\circ$ , the simulations overestimate  $C_d$ , though.

The way in which rotational effects influence the  $C_d$  characteristics of the MEXICO rotor blades differs from the descriptions found in the literature about this topic: as an example, in the NREL UAE Phase VI wind turbine, rotational effects were accompanied by a significant drag increase [16,18,29]. Additionally, Lindenburg [25] describes rotational effects to increase the drag as a consequence of the radial flows existing in rotating blades under stall conditions, arguing that energy is required for pumping air from the root region towards outer radial positions. Furthermore, most correction models for rotational effects predict a  $C_d$  increase [23–25], while others describe a  $C_d$  reduction [8,26] or no influence at all on  $C_d$  [21]. Owing to the fact that in the MEXICO turbine, rotational effects do not affect  $C_d$  substantially, except at  $r = 0.60R$ , it is not surprising that in the study by Guntur *et al.* [30], who tested different correction models with the MEXICO turbine, it is concluded that correcting for  $C_d$  might be unnecessary (their study was limited to the radial stations  $r = 0.25R$  and  $r = 0.35R$ ). That conclusion, which our results confirm for the same turbine, can however not be generalized for other wind turbines (as explained above). Furthermore, the fact that, in the MEXICO turbine, rotational effects influence  $C_d$  at  $r = 0.60R$ , but do not do it at  $r = 0.25R$  and  $r = 0.35R$ , is an indication that such effects might be airfoil type-dependent (at  $r = 0.25R$  and  $r = 0.35R$ , the DU91-W2-250 airfoil was used, whereas at  $r = 0.60R$ , the RISØ-A1-21 airfoil was utilized).

At  $r = 0.82R$ , as well as at  $r = 0.92R$  (Figure 2d,e, respectively), the experimental  $C_d$  from the 3D case is increased as compared with the 2D airfoil, especially at high AoA. The influence of the tip vortex and the subsequent downwash at radial positions  $r < R$  imply a reduction of the AoA, which also leads to a reduction of  $C_l$  and  $C_d$ . The  $C_d$  rise observed in the MEXICO turbine indicates that other influences must be taken into account. Lindenburg [25] suggested that the influence of the radial flows coming from inboard positions should be considered for modeling the airfoil characteristics at outboard positions. Therefore, his model for rotational effects includes a special correction for  $r > 0.8R$ , which is based on the idea that the spanwise flows acting on the separated volume of air can not be driven further outboard than the blade tip itself, which causes a pressure rise on the suction side of the tip region. As a consequence, he expected  $C_l$  and  $C_d$  to drop. This is in conflict with the  $C_d$  rise observed at high AoA in Figure 2d,e, so Lindenburg's suggestion does not seem adequate for the MEXICO wind turbine.

The CFD results for  $r = 0.82R$  and  $r = 0.92R$  present the problem that the drag is underpredicted at high AoA. Even for 2D airfoils, the prediction of the aerodynamic loads under stall conditions is known to be a challenge for RANS computations [50], so the mismatch with the experiments are probably due to the limitations of the RANS method. These limitations for the prediction of separated flows mainly arise from two issues: First, turbulence is not resolved, but modeled. The turbulence models are usually designed and calibrated for certain applications and conditions, and they are by no means universally reliable. Complex flow situations, like flow separation, are certainly a major challenge for any turbulence model. Secondly, RANS is not able to resolve the unsteadiness associated with separated flows, because it only provides an averaged solution, which of course can lead to poor predictions in the stall region. However, this problem is expected to be of less importance in the blade root region, where separation is

known to be a rather stationary process, because of the stabilizing standing vortex that characterizes stall in that part of the blade [9,51].

However, it remains unclear why under stall conditions the experimental results for  $r = 0.82R$  and  $r = 0.92R$  show that the lift reduction is accompanied by a drag increase as compared with the 2D airfoil. This problem is further discussed in the Sections 3.3 and 3.4.

### 3.2. Influence of Rotational Effects on the $C_p$ Distributions

The 3D airfoil characteristics have shown that, under stall conditions, stall delay and/or lift enhancement influence the aerodynamic performance of the blade at the radial positions  $r = 0.25R$ ,  $r = 0.35R$  and  $r = 0.60R$ . In order to study in more detail the origin of those effects, the computed and measured  $C_p$  distributions of the mentioned radial positions are presented in Figures 3–5 for  $U_\infty = 24$  m/s (corresponding to the wind speed at which the strongest rotational effects occur). In Figures 3 and 4 ( $r = 0.25R$  and  $r = 0.35R$ , respectively), the experimental  $C_p$  distributions from the corresponding 2D airfoil (DU91-W2-250) are also shown. Unfortunately, for the station  $r = 0.60R$ , which uses the airfoil RISØ-A1-21, no experimental  $C_p$  distribution of the 2D airfoil is available.

At  $r = 0.25R$  (Figure 3), the blade rotation induces two important effects on the suction side: the suction peak is enhanced, and the slope of the adverse pressure gradient is reduced. Both effects lead to a delay of the point of separation, which is the point where the adverse pressure gradient and the region with a constant, nearly zero pressure gradient meet [19]. In the 2D case, the separation point is located at  $x \approx 0.2c$ , whereas in the 3D experimental case it seems to be at  $x \approx 0.3c$ , although in this case, the change in slope, *i.e.*, pressure gradient, is more gradual, which complicates the exact determination of the separation point. Consequently, the lift in the 3D case is greatly enhanced (see also Figure 1a). The numerical results predict these phenomena very well, showing an excellent agreement with the 3D experimental results.

At  $r = 0.35R$  (Figure 4), evidence of rotational effects is present both in the experimental and numerical results, although their intensity is much lower than at  $r = 0.25R$ . The simulations clearly overpredict the stall delay effect, which according to the 3D experiments seems to be nearly negligible. Ultimately, this results in the overprediction of the computed  $C_l$  seen in Figure 1b. The  $C_l$  enhancement of the 3D experimental results with respect to the 2D experiments is caused by the magnified suction peak. Sicot *et al.* [11], who studied experimentally a 1.34-m rotor diameter wind turbine, also observed lift enhancement without evidence of stall delay at two radial positions ( $r = 0.26R$  and  $r = 0.50R$ ). The lack of stall delay was attributed to the high turbulence level of their experimental setup (TI = 9%). However, in the MEXICO experiment, the turbulence intensity was only TI = 0.8%, which contradicts their assumption. This leads to the conclusion that stall delay and  $C_l$  enhancement can exist independently of each other (although they are often observed together), no matter what the flow regime is.

At  $r = 0.60R$  (Figure 5), the agreement between experimental and numerical results is again excellent, and the  $C_p$  distribution resembles qualitatively those from  $r = 0.25R$  and  $r = 0.35R$ : a strong suction peak in the proximity of the leading edge is followed by an adverse pressure gradient and a region with nearly constant pressure, which extends until the trailing edge. This type of  $C_p$  distribution

is characteristic for 2D airfoils with trailing edge separation. Having such distributions in regions where rotational effects do not play any role is not surprising. However, in regions influenced by rotational effects, other  $C_p$  distribution shapes are usually expected. For instance, in the NREL UAE Phase VI turbine, the  $C_p$  curves from regions influenced by rotational effects exhibited no suction peak and no (or very weak) adverse pressure gradient [9]. In a more recent work, Schreck *et al.* [52] have highlighted that the MEXICO rotor blades do not exhibit those features. Ronsten [6] performed experiments on a 2.375-m rotor blade, and his results show that in regions affected by rotational effects, the  $C_p$  curves displayed a very reduced adverse pressure gradient extending uniformly from a broad suction peak until the trailing edge. Sicot *et al.* [11] also obtained similar  $C_p$  curves in their experimental study of rotational effects on a 1.34-m wind turbine rotor. On the other hand, the experimental and numerical study by Troldborg *et al.* [38] on the 3D airfoil characteristics of a multi-megawatt wind turbine showed  $C_p$  distributions from radial positions affected by rotational effects that resemble the results from the MEXICO turbine: the suction side exhibited a suction peak in the proximity of the leading edge; then the pressure was increased by an adverse pressure gradient; and finally, the pressure was kept nearly constant until the trailing edge.

One more interesting feature of the  $C_p$  distributions from Figures 3–5 is the fact that the pressure level in areas with separated flow, *i.e.*, regions from the suction side with nearly constant pressure, is very similar for the 2D and 3D cases. This is in conflict with the observations done by Schreck and Robinson [9] in the NREL Phase VI wind turbine, who observed that the pressure in the separated region was substantially reduced as compared with the 2D airfoil. Lindenburg [25] also analyzed the same measurements and concluded that radial flows in the separated flow region cause an important additional negative pressure, which contributes to the lift enhancement.

The lack of such a strong additional negative pressure in the separated regions of the MEXICO blades could be interpreted as a lack of substantial radial flows. However, as will be shown in Sections 3.3 and 3.4, this assumption does not hold true.

All of these observations show that there is not a unique shape of the  $C_p$  distribution that can be considered as representative for rotational effects. This hinders the development of generalized correction models that perform well for any kind of wind turbine.

**Figure 3.**  $C_p$  distribution from  $r = 0.25R$  for  $U_\infty = 24$  m/s, corresponding to  $\text{AoA} = 26^\circ$ . The dotted line represents 2D experimental results; the circles indicate 3D experimental results; and the full line shows 3D numerical results.

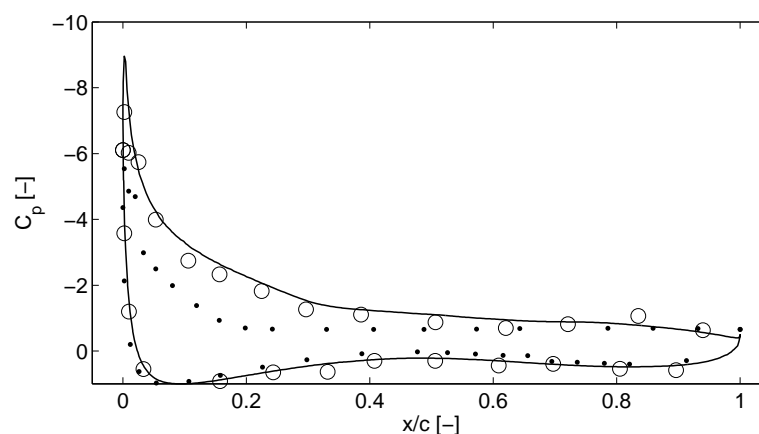


**Figure 4.**  $C_p$  distribution from  $r = 0.35R$  for  $U_\infty = 24$  m/s, corresponding to  $\text{AoA} = 23^\circ$ . The dotted line represents 2D experimental results; the circles indicate 3D experimental results; and the full line shows 3D numerical results.

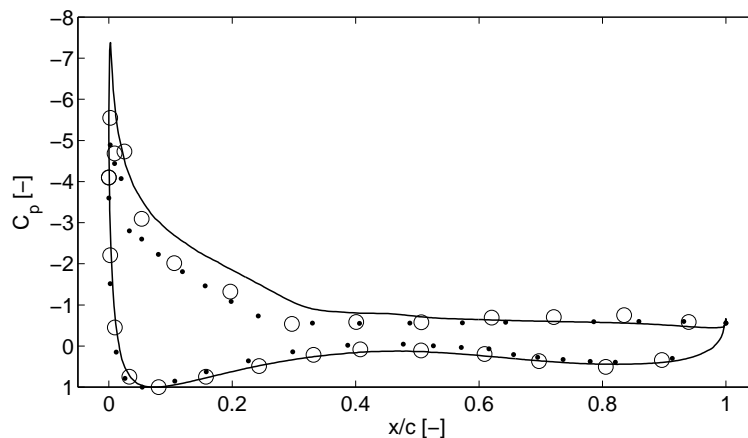
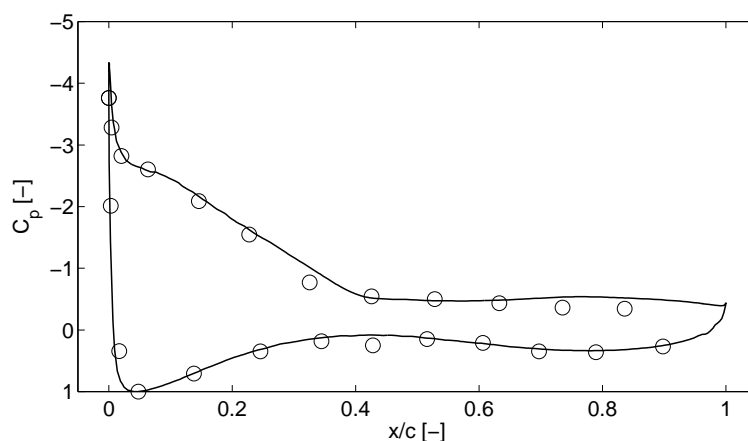


**Figure 5.**  $C_p$  distribution from  $r = 0.60R$  for  $U_\infty = 24$  m/s, corresponding to  $\text{AoA} = 17^\circ$ . The circles indicate 3D experimental results, and the full line shows 3D numerical results.



### 3.3. Flow Field in the Wake after the Blade Passage

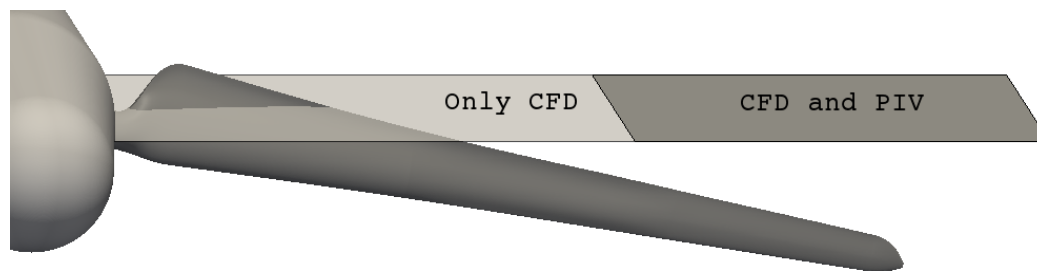
The study of the particle image velocimetry (PIV) experimental data in conjunction with the numerical results allows one to gain better insight into relevant flow features, which are important for the analysis of the rotational effects.

Figure 6 shows schematically the area where the flow field was experimentally captured by means of PIV measurements. The PIV sheets cover the range of radial positions  $0.52R < r < 1.21R$ , (where  $R$  represents the rotor radius and  $r$  the local radius) and the range of axial positions  $-0.13R < x < 0.13R$ , where  $x = 0R$  is the rotor plane (upstream of the rotor plane, the axial coordinates are negative, whereas downstream of it, they are positive). For radial positions lower than  $0.52R$ , only numerical data are available.

All of the presented results were acquired 10 degrees after the blade passage. The experimental data, which are available for the wind speeds 10, 15 and 24 m/s, are compared with the numerical results in Figures 7–9, respectively. The white regions observed in the numerical results correspond to the

intersection of the nacelle and the blade inboard region with the plane where the flow field is studied (the intersection is also displayed in Figure 6). All of the velocity fields shown in this analysis have been normalized with the free stream wind speed in order to make the comparison between the three different cases easier.

**Figure 6.** Schematic view of the plane where the flow field was measured  $10^\circ$  after the blade passage. The PIV windows only cover the outboard region, whereas the CFD results encompass the whole blade span.



**Figure 7.** Measured and computed flow field at  $U_\infty = 10$  m/s. (a) axial wind speed from experiments; (b) radial wind speed from experiments; (c) axial wind speed from simulations; (d) radial wind speed from simulations.

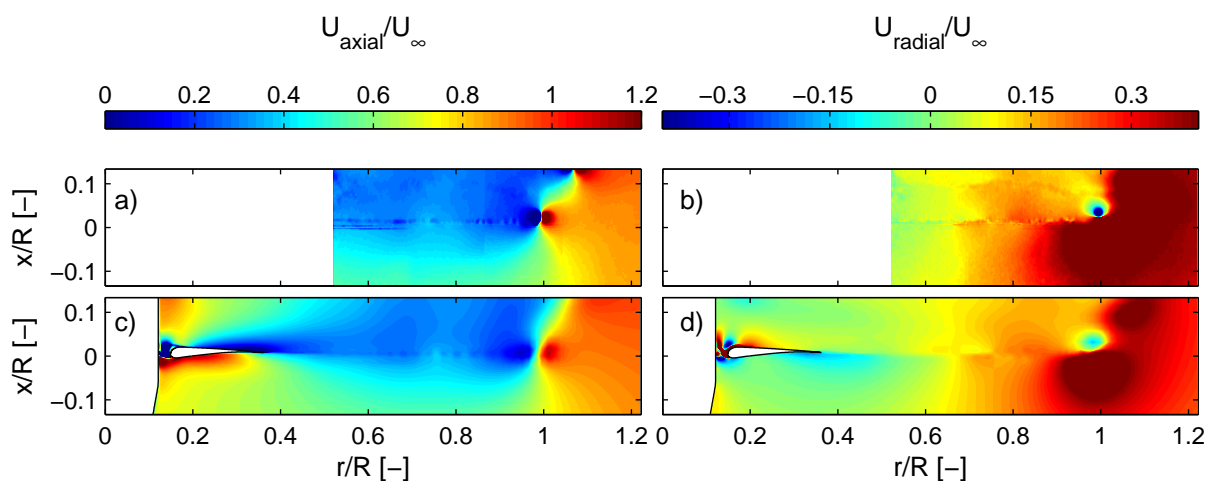
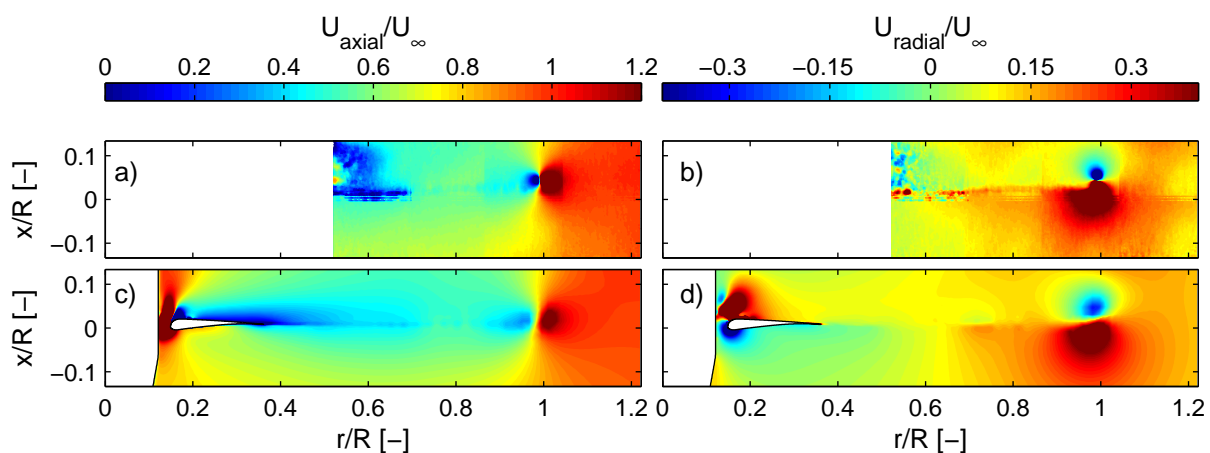


Figure 7a,c show respectively the measured and simulated axial wind speed for  $U_\infty = 10$  m/s. As can be seen, the axial wind speed in the rotor plane is about one third of the freestream velocity, indicating a high induction. The high induction leads to a strong wake expansion, which, in turn, is responsible for a significant radial component in the wind speed, especially in the blade outboard region, as presented in Figure 7b for the experiment and Figure 7d for the simulation. However, as can be seen in the wake, the passage of the blade does not trigger additional radial flows. This is an indication that at this wind speed, at which rotational effects are non-existent, the flow in the blade boundary layer is attached and 2D. The experimental and numerical results compare fairly well for both the axial and radial velocity components, although the simulation underpredicts the strength of the tip vortex a bit and the radial

velocity component for  $r > R$ . Interestingly, the numerical results show the existence of a substantial radial velocity component in the blade root region, which seems to suggest that the flow in that area is separated.

At  $U_\infty = 15$  m/s, the outboard region of the rotor plane presents an axial wind speed that almost reaches two thirds of the free-stream wind speed, indicating optimum induction (Figure 8a for the experiment and Figure 8c for the simulation). At inboard positions, the axial wind speed is lower, *i.e.*, the induction is higher, but it should be noted that at those spanwise positions, the influence of the blade body on the studied plane is much stronger, because of its proximity (Figure 6). The reduced induction as compared to the case with  $U_\infty = 10$  m/s implies less wake expansion, which also means that the radial velocity component in the outboard region becomes weaker (Figure 8b,d for the experimental and numerical results, respectively). The blade passage does not contribute to increasing significantly the radial velocity component in the wake, but the experimental results suggest that it triggers a very weak vortex sheet, which does not exist in the numerical results. These results imply that the flow in the boundary layer is basically attached and 2D, although incipient separation might exist close to the trailing edge. Apart from this, the agreement between numerical and experimental results is excellent in spite of some rather artificial effects in the experimental results in the range  $0.52R < r < 0.7R$ . Micallef *et al.* [53] attributed those effects to the laser sheet reflection on the blade. The root vortex is also easily recognizable in the radial component of the numerical results.

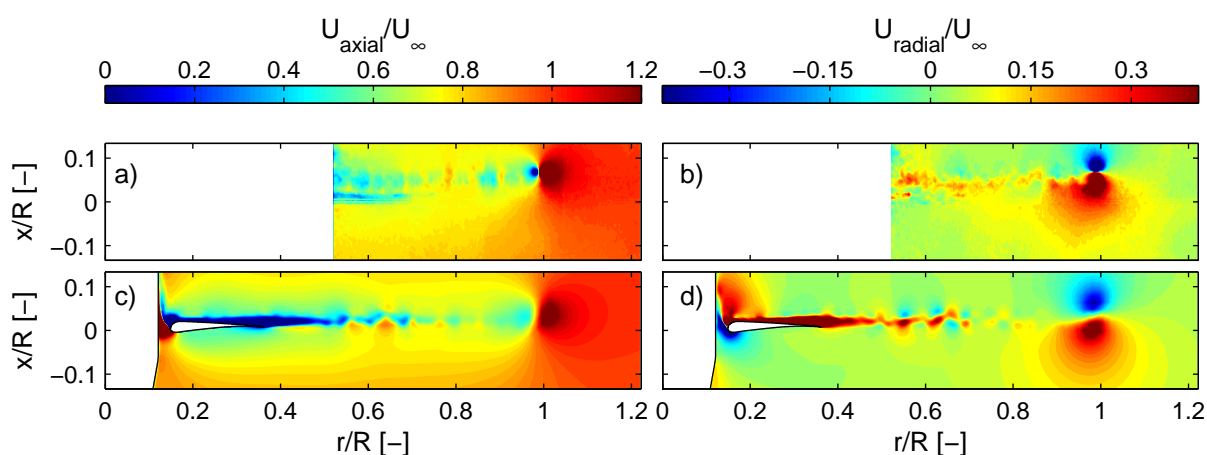
**Figure 8.** Measured and computed flow field at  $U_\infty = 15$  m/s. (a) axial wind speed from experiments; (b) radial wind speed from experiments; (c) axial wind speed from simulations; (d) radial wind speed from simulations.



From Figure 9a,c (experimental and numerical results, respectively), it is clear that at  $U_\infty = 24$  m/s, the axial induction is weaker than at  $U_\infty = 15$  m/s. This circumstance reduces the wake expansion and consequently also the radial velocity component promoted by the expansion itself (Figure 9b,d). However, the blade passage increases the radial velocity due to the trailed vorticity. This effect is visible in the experimental, as well as in the numerical results, in spite of some inconsistencies between both of them. Here, it is worth recalling that under these conditions (stall), the flow is non-stationary, and the

experimental results, which are phase-locked, are averaged over 30 frames, where a frame is the result of two subsequent photographs, *i.e.*, an image pair [36]. Therefore, after averaging the measured frames, the radial velocities appear as a smeared blob of spanwise flow along the blade radius. This poses a challenge for the comparison with the numerical results, because the simulations are steady-state, so only one solution is obtained and no averaging over time is possible. This problem is accentuated by the flapwise oscillations: as can be seen in the experimental results (Figure 9a,b), the axial position of the tip vortex is located further downstream than in the simulation (Figure 9c,d). In fact, the same happens at  $U_\infty = 10$  m/s and  $U_\infty = 15$  m/s, although the discrepancy increases with the wind speed. This seems to indicate that the blade presents a certain deflection in the flapwise direction when it is loaded. The experimental results (especially those corresponding to the axial velocity component; Figure 9a) also show that the vortex sheet located along the blade span is a bit bended towards the downstream direction, which confirms the blade deflection. Carrión *et al.* [54] performed a fluid-structure interaction study of the MEXICO turbine and estimated that the blade tip deflection was approximately 5 cm for  $U_\infty = 15$  m/s. For  $U_\infty = 24$  m/s, it should be even more. Under stall conditions, where the flow is highly nonstationary, the deflection is expected to be subjected to substantial flapwise oscillations. The corresponding oscillations in the wake, when averaged, contribute to the blurred distribution of radial velocities seen in the experimental results, complicating the comparison with the steady-state, rigid blade CFD simulation.

**Figure 9.** Measured and computed flow field at  $U_\infty = 24$  m/s. (a) axial wind speed from experiments; (b) radial wind speed from experiments; (c) axial wind speed from simulations; (d) radial wind speed from simulations.



In the range  $0.70R < r < 0.90R$ , the numerical results seem to underpredict the (weak) radial flow component. This is approximately the region where the experimental 3D airfoil characteristics are not consistent with the simulations and display a lift reduction and a drag increase with respect to the 2D case (Figures 1 and 2). The experimental radial velocity field seems to suggest that the reason for the underperformance of the blade in that region is connected to the increased trailed vorticity. However, it is not clear which is the source of the increased trailed vorticity: the NACA64-418 airfoil is used in

the range  $0.74R < r < R$ . Since there is no transition between different airfoil types in that region, no abrupt change in the bound circulation is expected there, meaning that no increased trailed vorticity is expected either. A possible torsional deflection caused by the pitching moment would act in the nose-down direction, which would reduce the AoA, decreasing at the same time the trailed vorticity. The effect can therefore not be explained by a torsional deflection. Furthermore, as described in Section 3.1, the influence of the tip vortex and the radial flows is not believed to be the cause for this aerodynamic behavior. Further insight is gained in the next section.

At lower radial positions, the numerical results are in better agreement with the measurements. In the inboard region, the analyzed plane intersects the blade, and the numerical results provide valuable information about the flow in the boundary layer. Figure 9d shows that the flow in this region, in which rotational effects play an important role, is dominated by a strong radial component (in contrast to the cases in which rotational effects were negligible). The fact that the rotational effects only exist in the presence of radial flows in the boundary layer suggests that most probably there is a connection between both phenomena. This is in conflict with the work of Wood [7], who concluded that rotational effects can be explained in terms of changes on the pressure gradient in the external inviscid flow. In other words, Wood suggested that inertial forces in the boundary layer (causing, e.g., radial flows) can be disregarded, because boundary layers respond to the pressure gradients imposed on them. On the contrary, other authors, like Dumitrescu and Cardus [55], have highlighted the importance of the blade boundary layer and the forces acting on it for the study of rotational effects.

### 3.4. Wall-Bounded Flow Field

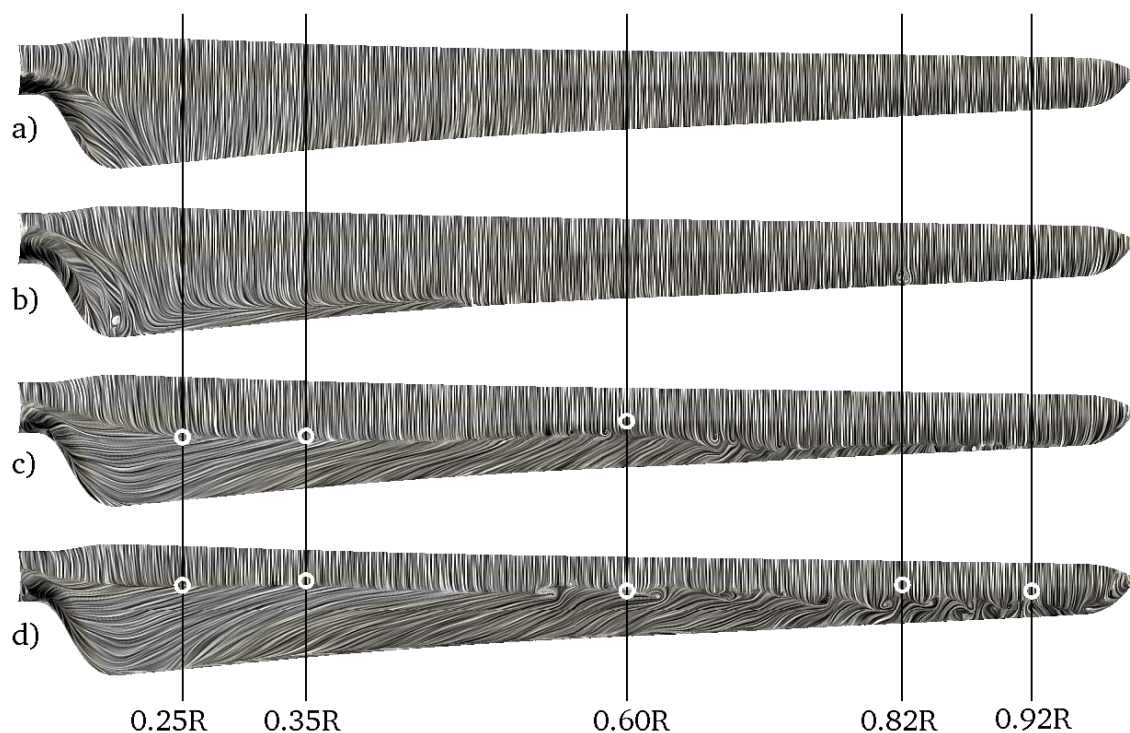
In order to analyze in more detail the wall-bounded flow field on the suction side, the simulated wall shear stress on the suction side is visualized as oil flow in Figure 10 for all of the computed wind speeds. Under stall conditions, the separation line is clearly recognizable along the span as the location where the flow coming from the leading edge ceases to be oriented in the chordwise direction. Furthermore, the figure shows with circles the separation point obtained from the experimental  $C_p$  distributions at five radial positions (in the cases where separation occurs). Here, it has been assumed that the location of the separation point corresponds to the point where the adverse pressure gradient meets the region with a constant, nearly zero pressure gradient [11,19].

At  $U_\infty = 10$  m/s and  $U_\infty = 15$  m/s (Figure 10a,b, respectively), the flow is almost fully attached and 2D. However, evidence of separation exists in the root region (around the area of maximum chord) in both cases. Furthermore, incipient flow separation is present in the inboard-aft region at 15 m/s. From the experimental results, it was not possible to determine clearly if there was separation at inboard positions, so no experimental separation point is shown for these wind speeds.

At  $U_\infty = 19$  m/s and  $U_\infty = 24$  m/s (Figure 10c,d, respectively), the blade is stalled to a great extent. At inboard and mid-span positions ( $r = 0.25R$ ,  $r = 0.35R$  and  $r = 0.60R$ ), the location of the computed separation line is consistent with the experimental separation point. However, at  $U_\infty = 24$  m/s, the experimental separation point from outboard radial positions ( $r = 0.82R$  and  $r = 0.92R$ ) is closer to the leading edge than in the simulations. As was seen in Figure 1d,e, the numerical results at these stations resemble approximately the 2D case for high AoA, so the measured underperformance of the

blade with respect to the 2D airfoil (Section 3.1) should be ascribed to the advancement of the separation point. Furthermore, this is also consistent with the  $C_d$  rise observed in Figure 2d,e and with the increased trailed vorticity described in Section 3.3. However, it is still not clear what exactly is causing this effect. Further research is therefore needed for explaining it.

**Figure 10.** Oil-flow representation of the computed wall shear stress on the suction side at different wind speeds: (a)  $U_\infty = 10$  m/s, (b)  $U_\infty = 15$  m/s, (c)  $U_\infty = 19$  m/s and (d)  $U_\infty = 24$  m/s. The white dots indicate the point of separation extracted from the experimental  $C_p$  distributions.



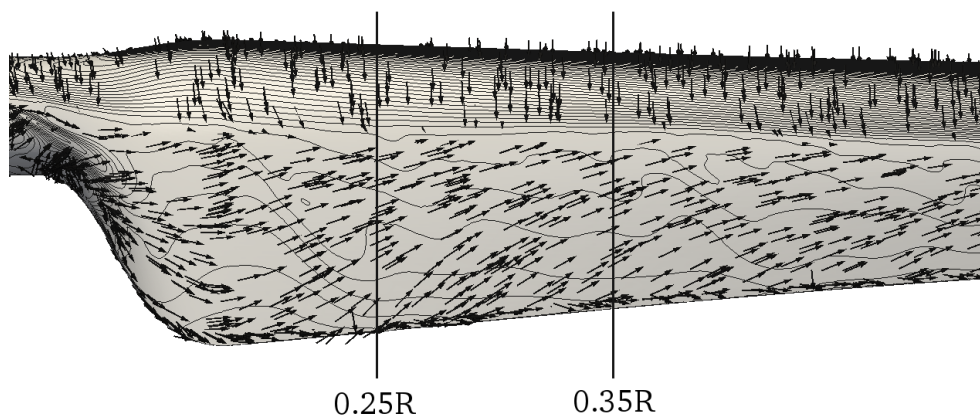
From Figure 10c,d, it is also evident that under stall conditions, large regions of the suction side are dominated by radial flows, which additionally contain a recirculation component towards the leading edge. The combination of the recirculation and the radial flow in the inboard region creates a standing vortex on the separated area, which “pumps” the air radially from the root region outwards. This effect, which is commonly referred to as “radial pumping”, has been observed both experimentally [5,51,56] and numerically [18,19] in other turbines operating under stall conditions, and it is usually considered to be intrinsically related to the existence of rotational effects.

Two main causes have been identified in the literature for explaining the origin of the radial flows in the boundary layer. The first explanation attributes the radial flows to the difference in dynamic pressure along the blade span. This pressure difference occurs because, for a given rotational speed, the local tangential speed is directly proportional to the local radius. Consequently, the air is supposed to travel from regions of high pressure (blade root) to regions of low pressure (blade tip). This explanation was supported by the observations done in the NREL UAE Phase VI wind turbine by Schreck and Robinson [9], who concluded that strong spanwise pressure gradients were responsible for the radial flows. The second explanation considers that the spanwise pressure gradients found on the separated

flow regions are too small for causing any radial flow, so it attributes the radial flows to the centrifugal force acting on the separated flow [25].

In Figure 11, the isobars obtained from the simulation with  $U_\infty = 24$  m/s are plotted together with arrows indicating the flow direction (extracted from the computed wall shear stress after inverting the sign).

**Figure 11.** Computed isobars of surface pressure and arrows indicating the flow direction at  $U_\infty = 24$  m/s. The isobars go from 0 to 8000 Pa with an interval of 80 Pa. The radial flow in the separated region is mostly unrelated to the pressure gradients.



From this figure, it is evident that the flow direction in the separated region is mostly unrelated to the pressure gradients. Consequently, in the MEXICO turbine, the radial flow in the boundary layer must be mainly attributed to the centrifugal force and not to spanwise pressure gradients. The fact that larger wind turbines rotate slower may lead to thinking that this effect could be much less pronounced in utility-scale wind turbines, since the centrifugal force is proportional to the square of the rotational speed and only linearly proportional to the radius. However, it must be kept in mind that the tip speed ratio for both small and large wind turbines is comparable, which should lead to similar effects of rotation (as was also explained in Section 2.1 with the Rossby number).

As often described in the literature about rotational effects [25,29], the Coriolis force acting on the separated radial flow apparently pushes that volume of air towards the trailing edge, which contributes to delaying the separation. Perhaps more importantly, the centrifugal force, which of course also acts on the attached flow region, gives the attached flow a radial velocity component in regions close to the end of the adverse pressure gradient, where the chordwise velocity component is very weak. The Coriolis force acting on that radial velocity component is also oriented towards the trailing edge, so it partially counteracts the adverse pressure gradient and, consequently, helps to delay separation before it happens at all. The fact that the Rossby number decreases towards the blade root (as seen in Table 2) suggests that Coriolis force plays a decisive role in the stall delay effect.

#### 4. Conclusions

In the current work, a CFD model of the MEXICO turbine based on the open source toolbox OpenFOAM, has been used in conjunction with experimental results for the study of rotational effects.

The closer to the blade root, the stronger was their influence on the aerodynamic performance. The evidence shows that the subsequent phenomena of stall delay and lift enhancement can exist independently of each other, although they tend to manifest themselves together. Furthermore, their influence on the drag seems to be airfoil-type dependent: the drag is not affected at positions where the DU91-W2-250 airfoil is used, but it is reduced at the radial position with the RISØ-A1-21 airfoil. It must be noticed that most correction models for rotational effects assume a drag increase, which is in conflict with our observations. In fact, the influence of rotational effects on the  $C_p$  distributions differs qualitatively very strongly from one turbine to the other, implying that no single shape of  $C_p$  distribution can be considered as representative for rotational effects. This is a major issue for the development of generalized correction models.

The use of flow field data from PIV experiments and numerical simulations allowed us to observe that the presence of a strong radial velocity component in the rotor plane does not lead to lift enhancement or stall delay as long as its origin is not in the blade boundary layer. On the other hand, the radial flows dominating the aft region of the boundary layer under stall conditions seem to be intrinsically connected to the existence of rotational effects. According to our results, these radial flows are due to the centrifugal force acting on the separated air volume, whereas in the literature of the NREL UAE Phase VI wind turbine, spanwise pressure gradients are mentioned to be responsible for the effect. Furthermore, the Coriolis force acting on the radial flow seems to play a crucial role in the stall delay effect.

These findings show the lack of generality of the state-of-the-art knowledge about rotational effects and stress the necessity for more research in this field.

## Acknowledgments

This work was financed by the Lower Saxony Ministry for Science and Culture. We thank the computer time provided by the Facility for Large-scale Computations in Wind Energy Research (FLOW) at the University of Oldenburg. The MexNext consortium is acknowledged for inspiring discussions. We are also grateful to Elia Daniele, Stefan Albensoeder and Wided Medjroubi for their valuable comments.

## Author Contributions

I.H. run the computations and wrote the manuscript. B.S. and J.P. supervised the work and contributed in the interpretation of the results.

## Conflicts of Interest

The authors declare no conflict of interest.

## References

1. Leishman, J.G. Challenges in modeling the unsteady aerodynamics of wind turbines. *Wind Energy* **2002**, *5*, 85–132.

2. Simms, D.; Schreck, S.; Fingeresh, L. *NREL Unsteady Aerodynamics Experiment in the NASA-Ames Wind Tunnel: A Comparison of Predictions to Measurements*; Technical Report NREL/TP-500-29494; National Renewable Energy Laboratory: Golden, CO, USA, 2001.
3. Himmelskamp, H. *Profile Investigations on a Rotating Airscrew*; Reports and translations; MAP Völenrode: Göttingen, Germany, 1947.
4. Banks, W.; Gadd, G. Delaying effect of rotation on laminar separation. *AIAA J.* **1963**, *1*, 941–942.
5. McCroskey, W.; Yaggy, P. Laminar boundary layers on helicopter rotors in forward flight. *AIAA J.* **1968**, *6*, 1919–1926.
6. Ronsten, G. Static pressure measurements on a rotating and a non-rotating 2.375 m wind turbine blade. Comparison with 2D calculations. *J. Wind Eng. Ind. Aerodyn.* **1992**, *39*, 105–118.
7. Wood, D. A three-dimensional analysis of stall-delay on a horizontal-axis wind turbine. *J. Wind Eng. Ind. Aerodyn.* **1991**, *37*, 1–14.
8. Du, Z.; Selig, M. The effect of rotation on the boundary layer of a wind turbine blade. *Renew. Energy* **2000**, *20*, 167–181.
9. Schreck, S.; Robinson, M. Rotational augmentation of horizontal axis wind turbine blade aerodynamic response. *Wind Energy* **2002**, *5*, 133–150.
10. Tangler, J.L. Insight into wind turbine stall and post-stall aerodynamics. *Wind Energy* **2004**, *7*, 247–260.
11. Sicot, C.; Devinant, P.; Loyer, S.; Hureau, J. Rotational and turbulence effects on a wind turbine blade. Investigation of the stall mechanisms. *J. Wind Eng. Ind. Aerodyn.* **2008**, *96*, 1320–1331.
12. Duque, E.P.N.; van Dam, C.; Hughes, S. Navier-Stokes Simulations of the NREL Combined Experiment Phase II Rotor. In Proceedings of the 1999 ASME Wind Energy Symposium, Reno, NV, USA, 11–14 January 1999; pp. 143–153.
13. Duque, E.P.N.; Burklund, M.D.; Johnson, W. Navier-Stokes and comprehensive analysis performance predictions of the NREL Phase VI experiment. *J. Sol. Energy Eng.* **2003**, *125*, 457–467.
14. Le Pape, A.; Lecanu, J. 3D Navier-Stokes computations of a stall-regulated wind turbine. *Wind Energy* **2004**, *7*, 309–324.
15. Johansen, J.; Sørensen, N.N.; Michelsen, J.A.; Schreck, S. Detached-eddy simulation of flow around the NREL Phase VI blade. *Wind Energy* **2002**, *5*, 185–197.
16. Johansen, J.; Sørensen, N.N. Aerofoil characteristics from 3D CFD rotor computations. *Wind Energy* **2004**, *7*, 283–294.
17. Sørensen, N.; Schreck, S. Computation of the National Renewable Energy Laboratory Phase-VI rotor in pitch motion during standstill. *Wind Energy* **2012**, *15*, 425–442.
18. Sørensen, N.N.; Michelsen, J.A.; Schreck, S. Navier-Stokes predictions of the NREL phase VI rotor in the NASA Ames 80 ft × 120 ft wind tunnel. *Wind Energy* **2002**, *5*, 151–169.
19. Schreck, S.J.; Sørensen, N.N.; Robinson, M.C. Aerodynamic structures and processes in rotationally augmented flow fields. *Wind Energy* **2007**, *10*, 159–178.
20. Guntur, S.; Sørensen, N.N. A study on rotational augmentation using CFD analysis of flow in the inboard region of the MEXICO rotor blades. *Wind Energy* **2014**, doi:10.1002/we.1726.

21. Snel, H.; Houwink, R.; van Bussel, G.; Bruining, A. Sectional prediction of 3D effects for stalled flow on rotating blades and comparison with measurements. In Proceedings of the 1993 European Community Wind Energy Conference, Lübeck-Travemünde, Germany, 8–12 March 1993; pp. 395–399.
22. Chaviaropoulos, P.K.; Hansen, M.O.L. Investigating three-dimensional and rotational effects on wind turbine blades by means of a quasi-3D Navier-Stokes solver. *J. Fluids Eng.* **2000**, *122*, 330–336.
23. Raj, N. An Improved Semi-Empirical Model for 3-D Post-Stall Effects in Horizontal Axis Wind Turbines. Master's Thesis, University of Illinois, Urbana-Champaign, IL, USA, 2000.
24. Bak, C.; Johansen, J.; Andersen, P. Three-dimensional corrections of airfoil characteristics based on pressure distributions. In Proceedings of the 2006 European Wind Energy Conference Scientific, Athens, Greece, 7 February–2 March 2006.
25. Lindenburg, C. *Investigation into Rotor Blade Aerodynamics*; Technical Report ECN-C03-025; ECN: Petten, The Netherlands, 2003.
26. Corrigan, J.; Schillings, H. Empirical model for stall delay due to rotation. In Proceedings of the American Helicopter Society Aeromechanics Specialists Conference 1994, San Francisco, CA, USA, 19–21 January 1994.
27. Tangler, J.; Selig, M. An evaluation of an empirical model for stall delay due to rotation for HAWTs. In Proceedings of the WindPower 97, Austin, TX, USA, 15–18 June 1997.
28. Du, Z.; Selig, M. A 3D stall-delay model for horizontal axis wind turbine prediction. In Proceedings of the 1998 ASME Wind Energy Symposium, Reno, NV, USA, 12–15 January 1998.
29. Breton, S.P.; Coton, F.N.; Moe, G. A study on rotational effects and different stall delay models using a prescribed wake vortex scheme and NREL phase VI experiment data. *Wind Energy* **2008**, *11*, 459–482.
30. Guntur, S.; Bak, C.; Sørensen, N. Analysis of 3D stall models for wind turbine blades using data from the MEXICO experiment. In Proceedings of the 13th International Conference on Wind Engineering, Amsterdam, The Netherlands, 10–15 July 2011.
31. Schepers, J.; Snel, H. *Model Experiments in Controlled Conditions, Final Report*; Technical Report ECN-E-07-042; ECN: Petten, The Netherlands, 2007.
32. Réthoré, M.; Zahle, F.; Sørensen, N.; Bechmann, A. CFD Simulations of the Mexico Wind Tunnel and Wind Turbine. In Proceedings of the European Wind Energy Association (EWEA) 2011, Brussels, Belgium, 14–17 March 2011.
33. Shen, W.Z.; Zhu, W.J.; Sørensen, J.N. Actuator line/Navier-Stokes computations for the MEXICO rotor: Comparison with detailed measurements. *Wind Energy* **2012**, *15*, 811–825.
34. Bechmann, A.; Sørensen, N.N.; Zahle, F. CFD simulations of the MEXICO rotor. *Wind Energy* **2011**, *14*, 677–689.
35. Jonkman, J.; Butterfield, S.; Musial, W.; Scott, G. *Definition of a 5 MW Reference Wind Turbine for Offshore System Development*; Technical Report NREL/TP-500-38060; NREL: Golden, CO, USA, 2009.
36. Boorsma, K.; Schepers, J. *Description of Experimental Setup. MEXICO Measurements*; Technical Report ECN-X09-0XX; ECN: Petten, The Netherlands, 2003.

37. Pascal, L. *Analysis of MEXICO Measurements*; Technical Report ECN-Wind Memo-09-010; ECN: Petten, The Netherlands, 2009.
38. Troldborg, N.; Bak, C.; Sørensen, N.; Madsen, H.; Réthoré, M.; Zahle, F.; Guntur, S. Experimental and numerical investigation of 3D aerofoil characteristics on a MW wind turbine. In Proceedings of the European Wind Energy Association (EWEA) 2013, Vienna, Austria, 4–7 February 2013.
39. Spalart, P.R.; Allmaras, S.R. A one-equation turbulence model for aerodynamic flows. *Rech. Aerosp.* **1994**, *1*, 5–21.
40. Spalding, D.B. A single formula for the law of the wall. *J. Appl. Mech.* **1961**, *28*, 444–458.
41. Rung, T.; Lübcke, H.; Thiele, F. Universal wall-boundary conditions for turbulence-transport models. *ZAMM J. Appl. Math. Mech./Z. Angew. Math. Mech.* **2001**, *81*, 481–482.
42. De Villiers, E. The Potential of Large Eddy Simulation for the Modelling of Wall Bounded Flows. Ph.D. Thesis, Imperial College London, London, UK, 2006.
43. Mockett, C. A Comprehensive Study of Detached-Eddy Simulation. Ph.D. Thesis, Technical University of Berlin, Berlin, Germany, 2009.
44. Schmidt, T.; Mockett, C.; Thiele, F. Adaptive Wall Function for the Prediction of Turbulent Flows. In *MEGADESIGN and MegaOpt—German Initiatives for Aerodynamic Simulation and Optimization in Aircraft Design*; Kroll, N., Schwamborn, D., Becker, K., Rieger, H., Thiele, F., Eds.; Notes on Numerical Fluid Mechanics and Multidisciplinary Design; Springer: Berlin, Germany, 2009; Volume 107, pp. 21–33.
45. Roache, P.J. Perspective: A Method for Uniform Reporting of Grid Refinement Studies. *J. Fluids Eng.* **1994**, *116*, 405–413.
46. Roache, P.J. Perspective: A Method for Uniform Reporting of Grid Refinement Studies. In *Computing in Science Engineering*; Hermosa Publishers: Socorro, NM, USA, 1998; pp. 8–9.
47. Hansen, M.; Sørensen, N.; Sørensen, J.; Michelsen, J. Extraction of lift, drag and angle of attack from computed 3D viscous flow around a rotating blade. In Proceedings of the Scientific from European Wind Energy Conference (EWEC), Dublin, Ireland, 6–9 October 1997; pp. 499–501.
48. Guntur, S.; Sørensen, N. An evaluation of several methods of determining the local angle of attack on wind turbine blades. In Proceedings of the Science of Making Torque from Wind 2012, Oldenburg (Oldb), Germany, 9–11 October 2012.
49. Schepers, J.; Boorsma, K.; Cho, T.; Gomez-Iradi, S.; Schaffarczyk, A.; Jeromin, A.; Shen, W.; Lutz, T.; Meister, K.; Stoevesandt, B.; et al. *Final Report of IEA Task 29, Mexnext (Phase 1): Analysis of Mexico Wind Tunnel Measurements*; Technical Report ECN-E12-004; ECN: Petten, The Netherlands, 2012.
50. Bertagnolio, F.; Sørensen, N.; Kohansen, J.; Fuglsang, P. *Wind Turbine Airfoil Catalogue*; Technical Report Risø-R-1280, Risø; Risø National Laboratory: Roskilde, Denmark, 2001.
51. Robinson, M.; Hand, M.; Simms, S.; Schreck, S. Horizontal axis wind turbine aerodynamics: Three-dimensional, unsteady, and separated flow influences. In Proceedings of the FEDSM99, San Francisco, CA, USA, 18–23 July 1999; Number FEDSM99-S295-01.

52. Schreck, S.; Sant, T.; Micallef, D. Rotational augmentation disparities in the MEXICO and UAE phase VI experiments. In Proceedings of the Science of Making Torque from Wind 2010, Heraklion, Greece, 28–30 June 2010.
53. Micallef, D.; van Bussel, G.; Ferreira, C.S.; Sant, T. An investigation of radial velocities for a horizontal axis wind turbine in axial and yawed flows. *Wind Energy* **2013**, *16*, 529–544.
54. Carrion, M.; Woodgate, M.; Steijl, R.; Barakos, G.; Gomez-Iradi, S.; Munduate, X. CFD and aeroelastic analysis of the MEXICO wind turbine. In Proceedings of the Science of Making Torque from Wind 2012, Oldenburg (Oldb), Germany, 9–11 October 2012.
55. Dumitrescu, H.; Cardos, V. Rotational effects on the boundary-layer flow in wind turbines. *AIAA J.* **2004**, *42*, 408–411.
56. Corten, G. Flow Separation on Wind Turbine Blades. Ph.D. Thesis, University of Utrecht, Utrecht, The Netherlands, 2001.

© 2014 by the authors; licensee MDPI, Basel, Switzerland. This article is an open access article distributed under the terms and conditions of the Creative Commons Attribution license (<http://creativecommons.org/licenses/by/4.0/>).